Astronomy & Astrophysics

The XMM deep survey in the CDF-S

II. A 9–20 keV selection of heavily obscured active galaxies at *z* > 1.7

K. Iwasawa[1], R. Gilli[2], C. Vignali[2,3], A. Comastri[2], W. N. Brandt[4,5], P. Ranalli[2,3,6], F. Vito[2,3], N. Cappelluti[2], F. J. Carrera[7], S. Falocco[7], I. Georgantopoulos[6], V. Mainieri[8], and M. Paolillo[9]

[1] ICREA and Institut de Ciències del Cosmos (ICC), Universitat de Barcelona (IEEC-UB), Martí i Franquès 1, 08028 Barcelona, Spain
  e-mail: `kazushi.iwasawa@icc.ub.edu`
[2] INAF – Osservatorio Astronomico di Bologna, via Ranzani 1, 40127 Bologna, Italy
[3] Università di Bologna – Dipartimento di Astronomia, via Ranzani 1, 40127 Bologna, Italy
[4] Department of Astronomy & Astrophysics, 525 Davey Lab, The Pennsylvania State University, University Park, PA 16802, USA
[5] Institute for Gravitation and the Cosmos, The Pennsylvania State University, University Park, PA 16802, USA
[6] Institute of Astronomy & Astrophysics, National Observatory of Athens, Palaia Penteli, 15236 Athens, Greece
[7] Instituto de Física de Cantabria (CSIC-UC), 39005 Santander, Spain
[8] European Southern Observatory, Karl-Schwarzschild-Straße 2, 85748 Garching, Germany
[9] Dipartimento di Scienze Fisiche, Università di Napoli Fedelico II, C.U. di Monte Sant'Angelo, via Cintia ed. 6, 80126 Napoli, Italy

ABSTRACT

We present results on a search of heavily obscured active galaxies $z > 1.7$ using the rest-frame $9-20$ keV excess for X-ray sources detected in the deep XMM-CDFS survey. Out of 176 sources selected with the conservative detection criteria ($>8\sigma$) in the first source catalogue of Ranalli et al. (in prep.), 46 objects lie in the redshift range of interest with the median redshift $\bar{z} \simeq 2.5$. Their typical rest-frame $10-20$ keV luminosity is 10^{44} erg s^{-1}, as observed. Among optically faint objects that lack spectroscopic redshift, four were found to be strongly absorbed X-ray sources, and the enhanced Fe K emission or absorption features in their X-ray spectra were used to obtain X-ray spectroscopic redshifts. Using the X-ray colour–colour diagram based on the rest-frame $3-5$ keV, $5-9$ keV, and $9-20$ keV bands, seven objects were selected for their $9-20$ keV excess and were found to be strongly absorbed X-ray sources with column density of $N_{\rm H} \geq 0.6 \times 10^{24}$ cm^{-2}, including two possible Compton thick sources. While they are emitting at quasar luminosity, $\sim 3/4$ of the sample objects are found to be absorbed by $N_{\rm H} > 10^{22}$ cm^{-2}. A comparison with local AGN at the matched luminosity suggests an increasing trend of the absorbed source fraction for high-luminosity AGN towards high redshifts.

Key words. galaxies: active – X-rays: galaxies

1. Introduction

A population of heavily obscured active galactic nuclei (AGN) at cosmological distances, which might be missed by conventional quasar surveys, has been postulated by AGN synthesis models of the X-ray background (XRB, e.g., Gilli et al. 2007; Treister et al. 2009a,b) and the super-massive black hole mass function in the local Universe (Marconi et al. 2004). Various infrared selections have been employed extensively for seaching for these objects in which strong re-radiation from obscuring dust is expected (Martínez-Sansigre et al. 2005; Alonso-Herrero et al. 2006; Daddi et al. 2007; Fiore et al. 2008, 2009; Bauer et al. 2010; Vignali et al. 2010; Alexander et al. 2011; Luo et al. 2011; Donley et al. 2012). Although X-ray observations should, in principle, also be effective for the search on account of the intrinsic X-ray loudness of AGN (relative to galaxy emission) and the penetrating power against obscuration, the low through-put of the existing X-ray telescopes limits the accessibility to high redshift. However, dedicated deep surveys with extremely long exposures, for example, in the *Chandra* Deep Field South (CDFS) conducted by *XMM-Newton* (Comastri et al. 2011) and *Chandra* (Giacconi et al. 2002; Xue et al. 2011) X-ray observatories now allow us to pursue this approach. Here, we present a

study of X-ray selected heavily obscured active galaxies using the 3 Ms *XMM-Newton* survey of CDFS.

X-ray absorption is measured by the low energy cut-off of an X-ray spectrum, which moves to higher energies as absorbing column density increases. When $N_{\rm H}$ approaches 10^{24} cm^{-2}, the cut-off occurs above 10 keV. As demonstrated for nearby examples, such as NGC 4945 (Iwasawa et al. 1993), the Circinus Galaxy (Matt et al. 1999a), and NGC 6240 (Vignati et al. 1999), detection of emission above 10 keV plays a key role in discoveries of heavily obscured AGN in those galaxies with absorbing column density exceeding 10^{24} cm^{-2}. This method works as long as the optical depth is not too large, that is, when a source becomes fully Compton thick with $N_{\rm H} \geq 10^{25}$ cm^{-2}, Compton down-scattering suppresses the hard X-rays, leaving only reflected light, as observed in NGC 1068 (e.g., Matt et al. 1997). While a direct access is not possible for nearby objects with *XMM-Newton*, this crucial energy-band is redshifted into its bandpass for high redshift objects at $z \geq 2$. Given the shape of an absorbed X-ray spectrum, a negative K-correction sustains the detectability of absorbed sources to high redshift. Utilizing these properties, we searched for the rest-frame $9-20$ keV excess sources to identify heavily obscured AGN candidates in the sources detected in the XMM-CDFS field.
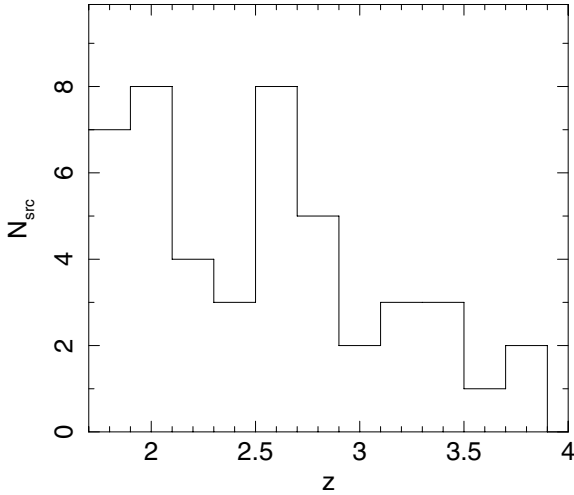
Fig. 1. Distribution of redshifts of the 46 sources in the sample. PID 352 with X-ray determined redshift $z_X = 1.60$ is excluded.

The cosmology adopted here is $H_0 = 70$ km s^{-1} Mpc^{-1}, $\Omega_\Lambda = 0.72$, $\Omega_M = 0.28$.
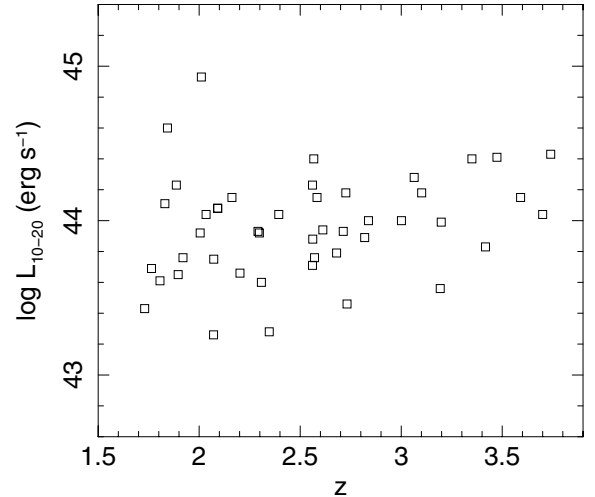
2. The sample

We selected sources from the first XMM-CDFS catalogue with conservative detection criteria: 176 sources that were detected at significance larger than 8σ in the 2−10 keV band and have X-ray spectra verified for use for a spectral analysis are available (details will be described in Ranalli et al., in prep.). Since the signal to noise ratio of individual spectra, obtained from the EPIC cameras of *XMM-Newton*, falls steeply above 7.5 keV, we set the lower bound of the redshift range of our sample to $z = 1.7$, for which rest-frame 20 keV corresponds to observed-frame 7.4 keV.

There are 47 objects with $z > 1.7$ for which spectral data are available from all the three EPIC cameras, pn, MOS1 and MOS2, apart from two objects which are located outside the field of view of the pn but within the two MOS cameras (see Table 1). Spectroscopic redshifts are available for 33 objects, while photometric redshifts were estimated by various papers (Luo et al. 2010; Cardamone et al. 2008; Rafferty et al. 2011; Wuyts et al. 2008; Santini et al. 2009; Taylor et al. 2009) for other 14 objects[1].

For some objects with photometric redshifts, more constrained redshift estimates could be obtained using the Fe K feature in their X-ray spectra when they have a strongly absorbed X-ray spectrum. We use these X-ray redshifts for five sources (Sect. 3.2). As a result of X-ray redshift determination, one source ($z = 1.60$), which had the original photometric redshift $z = 1.78$, went out of the redshift range. This source (PID 352) is therefore excluded from the sample and will not be discussed further.

Hereafter we use "PID" for the identification number of X-ray sources listed in Ranalli et al, and the basic information of the 46 objects in the sample is presented in Table 1. The redshift distribution of the sample is shown in Fig. 1. The median redshift is $\tilde{z} = 2.5$. The background-corrected counts obtained from the the sum of the three EPIC cameras range from 400

---

[1] The photometric redshift adopted in this paper are taken from Ranalli et al. (in prep.), in which the choices among various photometric redshift estimates are described in detail.

Fig. 2. Distribution of the 46 objects in our sample in the rest-frame 10−20 keV luminosity vs. redshift plane. No correction for internal absorption has been made when calculating the luminosities. The median $\tilde{L}_{10-20}$ is 0.9×10^{44} erg s^{-1}.

to 8000 in the respective rest-frame 3−20 keV band, while the typical counts are ∼1400. The typical source fraction of the total (source plus background) counts is ≃0.4 in both EPIC pn and MOS cameras.

Since the exposure time for each source varies, the observed flux in the observed-frame 1−4 keV band, which is shared by all the sources with various redshifts, is given in Table 1 as an objective measure of source brightness. Median values of the observed frame 1−4 keV flux, f_{1-4}, the rest-frame 2−10 keV and 10−20 keV luminosities, L_{2-10}, and L_{10-20}, are 2.5×10^{-15} erg s^{-1} cm^{-2}, 9.1×10^{43} erg s^{-1}, and 8.7×10^{43} erg s^{-1}, respectively. These luminosities are corrected for the Galactic extinction, $N_H = 9 \times 10^{19}$ cm^{-2} (Dickey & Lockman 1990). Figure 2 shows how the objects in our sample are distributed in the $L_{10-20} - z$ plane. The spread of the 10−20 keV luminosity is relatively narrow with a logarithmic dispersion of 0.3 (or a factor of ∼2).

3. Results

3.1. X-ray colour analysis

For selecting sources with various degrees of absorption, three rest-frame energy bands: s (3−5 keV); m (5−9 keV); and h (9−20 keV), are defined and two X-ray colours: s/m and h/m are computed. At energies above 3 keV, little contribution from soft X-ray emission originating from the extranuclear region is expected. As the intrinsic continuum slope in the 3−20 keV band is not expected to vary wildly between objects, absorption would be the main driver of changes in the X-ray colours. For the adopted rest-frame energy range, these X-ray colours are sensitive to column densities larger than $N_H \simeq 10^{22}$ cm^{-2}.

Since our objects have a wide range of redshift (1.7−3.8 in z), these X-ray colours are derived using photon spectra, i.e., spectral data corrected for the detector response and the Galactic absorption as a function of the rest-frame energy. The correction method employed here is practically the same as that used in the XMM-COSMOS spectral stacking analaysis (Iwasawa et al. 2012). The photon counts in each band are the weighted mean of the three EPIC cameras, where we adopted the signal-to-noise ratio in the rest-frame 3−20 keV band as the weight. The two

Table 1. Properties of the sample.

PID (1)	RA (2)	Dec (3)	z (4)	(5)	(6)	Net (7)	s/m (8)	h/m (9)	(10)	f_{1-4} (11)	L_{2-10} (12)	L_{10-20} (13)
26	53.21484	−27.97884	3.198	sp	a	618	0.35 ± 0.17	0.97 ± 0.33	A	1.7e-15	9.2e+43	9.7e+43
30	53.03737	−27.97493	1.830	x	–	1344	0.29 ± 0.08	2.06 ± 0.27	V	2.5e-15	4.5e+43	1.3e+44
31	53.28854	−27.97376	2.583	sp	a	789	1.03 ± 0.15	1.07 ± 0.19	M	3.9e-15	2.1e+44	1.4e+44
33	53.25708	−27.97188	1.843	sp	a, b	8112	1.20 ± 0.04	0.77 ± 0.05	U	2.5e-14	6.8e+44	4.0e+44
49	52.97654	−27.94723	2.298	sp	c	1474	1.09 ± 0.14	1.07 ± 0.18	M	2.8e-15	1.0e+44	8.4e+43
57	53.29041	−27.93768	2.571	sp	a	1891	1.49 ± 0.14	0.68 ± 0.12	U	2.8e-15	1.8e+44	5.7e+43
62	53.30284	−27.93094	2.561	sp	a	3642	1.40 ± 0.08	0.60 ± 0.07	U	6.1e-15	3.8e+44	1.7e+44
64	53.17001	−27.92967	3.350	x	–	1277	0.23 ± 0.11	1.95 ± 0.31	V	2.5e-15	8.7e+43	2.5e+44
68	53.25377	−27.92238	2.005	sp	d	3023	1.30 ± 0.10	0.75 ± 0.11	U	5.5e-15	2.0e+44	8.4e+43
81	52.93824	−27.90995	1.887	sp	d	5524	1.37 ± 0.07	1.03 ± 0.09	U	1.1e-14	3.1e+44	1.7e+44
84	53.06075	−27.90602	2.561	sp	e	1226	0.99 ± 0.19	1.54 ± 0.31	M	1.3e-15	5.9e+43	5.1e+43
92	53.02137	−27.89840	3.417	ph	f	1066	0.90 ± 0.13	0.91 ± 0.16	M	1.1e-15	9.0e+43	6.7e+43
93	53.00222	−27.89788	2.819	ph	g	995	0.65 ± 0.13	1.05 ± 0.22	M	1.5e-15	7.2e+43	7.7e+43
97	53.19526	−27.89280	2.732	ph	h	441	0.18 ± 0.12	0.75 ± 0.24	A	6.8e-16	3.0e+43	2.9e+43
98	53.01620	−27.89159	3.001	ph	f	1411	0.88 ± 0.13	0.79 ± 0.15	M	1.3e-15	9.3e+43	1.0e+44
103	52.94689	−27.88717	2.034	ph	g	3901	1.17 ± 0.07	0.94 ± 0.08	U	6.4e-15	2.2e+44	1.1e+44
107	52.20927	−27.88088	3.474	sp	c	2468	0.78 ± 0.06	1.01 ± 0.07	M	3.7e-15	2.9e+44	2.6e+44
108	53.05395	−27.87688	2.562	sp	e	1164	0.45 ± 0.06	1.19 ± 0.13	A	1.6e-15	5.7e+43	7.5e+43
114	53.32027	−27.87144	1.806	sp	a	508	0.09 ± 0.20	1.92 ± 0.61	V	1.0e-15	2.2e+43	4.1e+43
116	53.04742	−27.87028	3.740	x	–	2176	0.45 ± 0.05	1.18 ± 0.08	A	3.0e-15	1.9e+44	2.7e+44
120	53.17388	−27.86740	3.591	sp	e	1987	1.24 ± 0.10	0.95 ± 0.09	U	2.1e-15	2.5e+44	1.4e+44
144	53.12423	−27.85159	3.700	sp	e	752	0.29 ± 0.16	1.46 ± 0.33	V	1.0e-15	4.2e+43	1.1e+44
158	52.96872	−27.83828	2.394	sp	e	1331	0.65 ± 0.09	1.34 ± 0.15	M	2.4e-15	8.2e+43	1.1e+44
173	53.18078	−27.82065	1.920	sp	e	2951	1.14 ± 0.07	0.80 ± 0.07	U	3.5e-15	1.1e+44	5.7e+43
180	53.16528	−27.81382	3.064	sp	e	1427	0.22 ± 0.05	2.01 ± 0.18	V	2.2e-15	7.4e+43	1.9e+44
190	53.26092	−27.80650	3.101	ph	f	1965	1.05 ± 0.08	0.87 ± 0.08	M	2.8e-15	2.1e+44	1.5e+44
194	53.03947	−27.80214	2.838	sp	b, e	1464	0.49 ± 0.05	1.03 ± 0.08	A	2.2e-15	1.1e+44	1.0e+44
200	53.24949	−27.79664	2.567	sp	e	6545	1.35 ± 0.05	0.75 ± 0.04	U	8.1e-15	5.1e+44	2.5e+44
201	52.91637	−27.79593	2.713	sp	d	1457	1.42 ± 0.13	0.78 ± 0.11	U	2.6e-15	2.0e+44	8.6e+43
210	53.17847	−27.78400	3.193	sp	e	1106	1.04 ± 0.16	0.69 ± 0.17	M	9.5e-16	8.7e+43	3.6e+43
211	53.03384	−27.78214	2.612	sp	c	1675	1.07 ± 0.10	1.01 ± 0.12	M	2.3e-15	1.1e+44	8.7e+43
213	53.27462	−27.78054	2.202	ph	f	1008	0.92 ± 0.17	0.99 ± 0.25	M	1.4e-15	4.6e+43	4.6e+43
215	53.02193	−27.77877	2.071	sp	c	690	0.12 ± 0.08	0.86 ± 0.16	A	1.1e-15	2.7e+43	4.0e+43
219	52.95665	−27.77598	2.308	sp	d	1042	1.65 ± 0.30	0.96 ± 0.27	U	1.6e-15	7.5e+43	4.0e+43
231	53.09398	−27.76715	1.730	sp	d	1111	0.64 ± 0.09	1.15 ± 0.18	M	1.2e-15	2.4e+43	2.7e+43
245	53.08279	−27.75493	2.680	x	–	373	0.08 ± 0.13	2.23 ± 0.54	V	7.9e-16	2.3e+43	6.1e+43
252	53.08340	−27.74644	1.896	sp	d	441	0.09 ± 0.15	2.44 ± 0.59	V	7.8e-16	1.9e+43	4.5e+43
269	53.37135	−27.73200	1.764	ph	g	663	0.93 ± 0.16	1.20 ± 0.28	M	2.8e-15	5.9e+43	4.9e+43
283	53.10732	−27.71837	2.291	sp	e	2076	0.84 ± 0.08	1.10 ± 0.12	M	2.7e-15	8.7e+43	8.6e+43
285	53.28673	−27.71504	2.072	sp	d	1798	1.37 ± 0.14	0.76 ± 0.15	U	3.3e-15	1.2e+44	5.6e+43
302	53.39597	−27.70256	2.011	sp	a	4054†	1.19 ± 0.05	0.83 ± 0.06	U	4.3e-14	1.4e+45	8.6e+44
311	53.25599	−27.69488	2.091	sp	i	3351	1.08 ± 0.07	1.06 ± 0.10	M	5.7e-15	1.8e+44	1.2e+44
327	53.37052	−27.67841	2.162	sp	d	638	0.74 ± 0.12	0.63 ± 0.16	M	5.0e-15	1.8e+44	1.4e+44
332	53.37428	−27.66908	2.092	sp	d	510†	0.78 ± 0.12	0.51 ± 0.15	M	5.6e-15	1.7e+44	1.2e+44
366	53.07546	−27.61604	2.347	ph	g	882	1.47 ± 0.26	1.37 ± 0.30	U	1.6e-15	7.6e+43	1.9e+43
503	53.00248	−27.72286	2.726	sp	e	2330	0.96 ± 0.06	0.82 ± 0.06	M	3.8e-15	2.3e+44	1.5e+44

Notes. (1) Source identification number in the XMM-CDFS catalogue of Ranalli et al.; (2), (3) XMM position of source (degrees, J2000); (4) redshift; (5) source of redshift, sp: optical spectroscopic; ph: photometric; x: X-ray spectroscopic; (6) references for the redshift estimates: a: Treister et al. (2009b); b: Cooper et al. (2012); c: Popesso et al. (2009); d: Silverman et al. 2010; e: Szokoly et al. (2004); f: Luo et al. (2010); g: Cardamone et al. (2008); h: Rafferty et al. (2011); and i: Balestra et al. (2010); (7) net counts in the rest-frame 3−20 keV band from all the three EPIC cameras. † MOS1+MOS2 only; (8) X-ray colour, s/m: photon ratio of the rest-frame 3−5 keV and 5−9 keV; (9) X-ray colour, h/m, photon ratio of the rest-frame 9−20 keV and 5−9 keV; (10) X-ray colour category; (11) observed-frame 1−4 keV flux in units of erg s^{-1} cm^{-2}; (12) rest-frame 2−10 keV luminosity in units of erg s^{-1}; (13) rest-frame 10−20 keV luminosity in units of erg s^{-1}. The luminosities given here are corrected for the Galactic absorption.

X-ray colours, s/m and h/m, for individual sources are listed in Table 1, and the colour–colour diagram is shown in Fig. 3.

With the two X-ray colours, a column density range of log $N_H = 22-24$ (cm^{-2}) can be probed, as s/m covers the lower N_H regime and h/m does the higher. In Fig. 3, a locus of spectral evolution when a power-law continuum of photon index $\Gamma = 1.8$ is modified by various absorbing column of log N_H between 21 and 24 (cm^{-2}) is drawn. As the s/m represents softness of a spectrum below 9 keV, objects at the bottom-right in Fig. 3 are populated by sources with little absorption. The s/m colour moves to the left as absorption increases. Two divisions were made along the s/m axis, at $s/m = 0.6$ and 1.1. In the lowest interval, the model locus turns upwards as increasing absorption at log $N_H \geq 23.5$ (cm^{-2}) and a few sources indeed
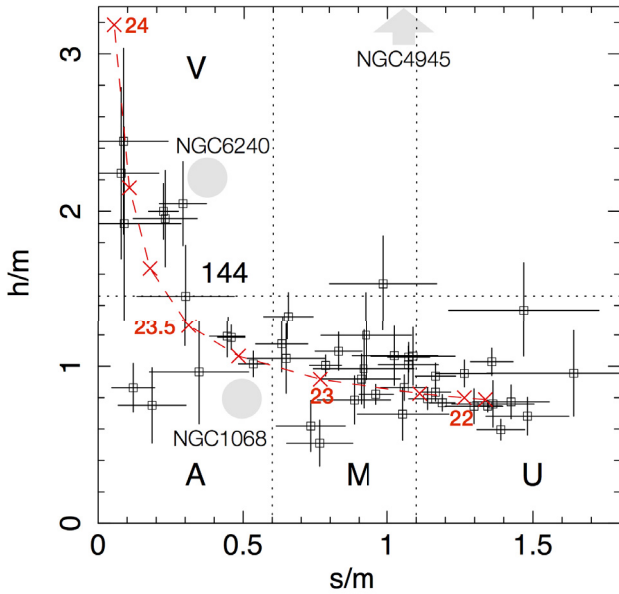
Fig. 3. X-ray colour–colour diagram, based on the data obtained from the *XMM-Newton* EPIC cameras, where s, m and h are the detector-response-corrected photon counts in the rest-frame bands of $3-5$ keV, $5-9$ keV and $9-20$ keV, respectively. The four categories, V, A, M and U and their boundaries are indicated. Our reference heavily obscured AGN, PID 144, is labeled in the diagram. The red dashed-line indicates the evolution track of the X-ray colour when a power-law of $\Gamma = 1.8$ is modified by various absorbing column. The crosses mark log $N_{\rm H}$ values 21, 22, 22.5, 23, 23.3, 23.5, 23.7, 23.85 and 24 (cm^{-2}) from the bottom-right to the upper-left along the track. The X-ray colours estimated for the nearby, heavily obscured AGN, NGC 6240, NGC 4945 and NGC 1068 are also plotted. Note that NGC 4945 has a large value of $h/m = 6.8$, which is outside of the frame (see text for details of these sources). X-ray spectra of the two sources (PID 84 and 366) with $h/m \sim 1.4$, located in the M and U intervals, respectively, are described in text (Sect. 3.1).

spread towards higher h/m values, which indicates an excess of $9-20$ keV emission.

PID 144 ($z = 3.70$) is a previously known, heavily obscured AGN with an X-ray absorbing column of $N_{\rm H} \sim (0.6-0.9)\times10^{24}$ cm^{-2} (Norman et al. 2002; Comastri et al. 2011), located in this interval. We take this object with $h/m = 1.46$ as the reference and sources that have h/m larger than this object were classified as $9-20$ keV excess sources.

According to the three intervals along s/m and two intervals along h/m, four zones, V: Very absorbed; A: Absorbed; M: Modestly absorbed; and U: Unabsorbed, are defined in the colour–colour diagram, as shown in Fig. 3. The degree of absorption thus increases in the order of U, M, A, and V, and typical column densities for these X-ray colour categories would be log $N_{\rm H}$ of ≤ 22, 22.7, 23.4, and 23.8 (cm^{-2}), respectively.

For a comparison, the X-ray colours of nearby, well-studied heavily obscured AGN, NGC 6240 ($N_{\rm H} \sim 2 \times 10^{24}$ cm^{-2}), NGC 4945 ($N_{\rm H} \sim 5 \times 10^{24}$ cm^{-2}), and NGC 1068 ($N_{\rm H} \geq 10^{25}$ cm^{-2}) were computed, based on the spectra presented in Vignati et al. (1999), Guainazzi et al. (2002), and Matt et al. (1997), respectively, obtained from the BeppoSAX observations (see Fig. 3). In these low luminosity systems, non AGN components, e.g., a circumnuclear starburst, flaring X-ray binaries (e.g., Brandt et al. 1996), can make a significant contribution to their spectra in the lower energy range, altering the s/m colour in particular, more than in high luminosity AGN like our sample.

Table 2. Properties of the four X-ray colour categories, V, A, M, and U.

Category	N	$\tilde{z}$	log $\tilde{L}_{2-10}$	log $\tilde{L}_{10-20}$	Γ_{10-20}
(1)	(2)	(3)	(4)	(5)	(6)
V	7	2.68	43.59	44.04	0.3 ± 0.2
A	6	2.78	43.86	43.93	1.5 ± 0.3
M	19	2.56	43.96	43.93	1.3 ± 0.2
U	14	2.19	44.20	43.99	1.6 ± 0.1

Notes. (1) The X-ray colour category (see Fig. 3); (2) number of objects belonging to the category; (3) median redshift; (4) median rest-frame $2-10$ keV luminosity; (5) median rest-frame $10-20$ keV luminosity; (6) photon index in the $10-20$ keV band of the stacked spectrum (see Fig. 3). Photon index Γ is related to the energy index α, where flux density, $F_{\rm E} \propto E^{-\alpha}$, by $\Gamma = \alpha + 1$.

Despite of this spectral complexity, h/m serves as a good indicator of strongly absorption seen in sources like NGC 6240 and NGC 4945. The h/m colour moves back to a lower value for a fully Compton thick source, e.g., NGC 1068, but it still remains in a zone of hard spectrum sources.

Two sources, PID 84 and PID 366, have h/m values similar to the reference PID 144 but softer s/m colours (see Table 1). An inspection of their spectra shows that PID 84 has a moderately absorbed spectrum with $N_{\rm H} \simeq 1 \times 10^{23}$ cm^{-2} as expected for the M category, while PID 366 in the U interval shows a relatively soft spectrum but with a deficit at the rest-frame $7-10$ keV (observed $2.2-3$ keV range), causing the large value of h/m. This could be attributed to a strong Fe K edge caused by absorption of $N_{\rm H} \sim 6 \times 10^{23}$ cm^{-2}, where a spectral complexity might play a role to mask the strong absorption.

The sources in the V and A categories are absorbed by $N_{\rm H}$ of a few times of 10^{23} cm^{-2} or larger, so that prominent Fe K features in the form of an emission line or an absorption edge can be observed. This offers a possibility to derive a reliable X-ray spectroscopic redshift. There are five objects in the two categories with only photometric redshifts. X-ray redshift ($z_{\rm X}$) were obtained for these five objects and their X-ray colours were recomputed assuming the new redshifts. Details of the X-ray redshift measurements are described in Sect. 3.2.

Basic information on the sources in the four categories is given in Table 2 and their stacked, rest-frame $3-20$ keV spectra are shown in Fig. 4, which demonstrates representative spectral shapes for respective categories. Note that exceptionally hard $10-20$ keV spectrum of V compared to the other three, indicating that large absorption column ($N_{\rm H} \sim 10^{24}$ cm^{-2}) are affecting the sources in this category (Table 2).

3.2. X-ray redshift measurements

Redshift was measured with X-ray spectra for five objects, PID 30, 64, 116, 245, and 352, which have only photometric redshifts (Table 3). These objects are too faint in the optical band to obtain a reliable spectroscopic redshift. The photometric redshifts reported by various authors for each object spread over a significant range, while they can serve as a guide for a redshift range to be searched in. The Fe K features imprinted in their absorbed spectra gave improved accuracy in the redshift measurements. The *Chandra* data from the 4 Ms (Xue et al. 2011) and the ECDFS (Lehmer et al. 2005) observations were also added to the analysis for improving the spectral quality. The observed-frame $0.5-7$ keV spectra of these sources are shown in Fig. 5, except for PID 352, details of which will be
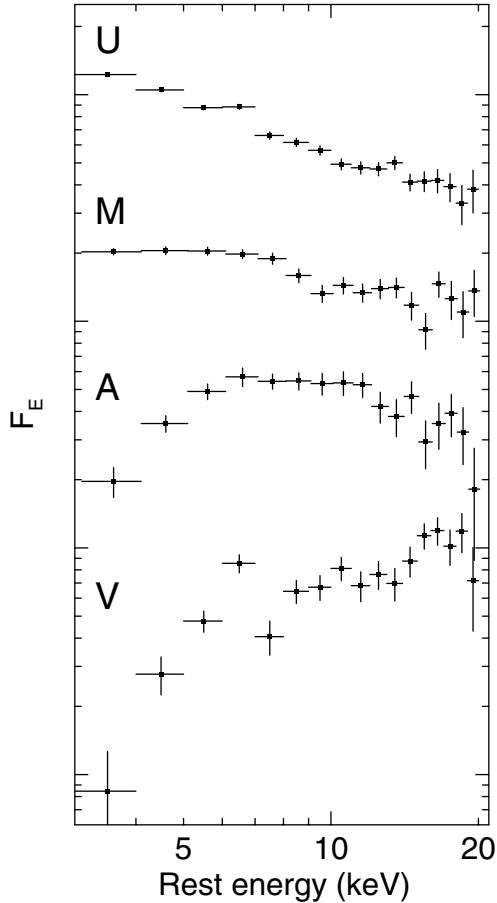
Fig. 4. Rest-frame 3−20 keV stacked spectra for the four categories, defined in Fig. 3. The vertical axis is in arbitrary unit of flux density. Only the *XMM-Newton* data were used. The spectral stacking is a straight sum of individual sources while a weighted mean of the available EPIC data, based on the signal to noise ratio, is taken for each source. Number of sources, typical redshift and luminosity of each category can be found in Table 2. For a reference, the spectral slope of the U category spectrum is $\alpha \simeq 0.8$, where $F_E \propto E^{-\alpha}$, i.e., photon index $\Gamma \simeq 1.8$.

Table 3. X-ray redshift measurements.

PID	z_X	Photo-z
30	1.83 ± 0.07	2.123^a, 1.936^b, 1.84^c, 1.683^d
64	3.35 ± 0.04	3.528^a, 3.341^c, 3.301^e
116	3.74 ± 0.06	3.53^a, 3.99^b, 4.63^f, 4.14^g
245	2.68 ± 0.12	3.001^a, 2.431^h, 2.28^k
352	1.60 ± 0.02	1.78^d

Notes. z_X is the X-ray spectroscopic redshift with 1σ error. The Fe K features are assumed to arise from cold matter (see text for details).

References. References for photometric redshifts a: Luo et al. (2010); b: Cardamone et al. (2008); c: Rafferty et al. (2011); d: Taylor et al. (2009); e: Wuyts et al. (2008); f: Wardlow et al. (2011); g: Wardlow et al. (2011, the second solution); h: Dahlen et al. (2010); k: Santini et al. (2009).

reported in a separate paper. They are photon spectra combining *XMM-Newton* and *Chandra* data for displaying purpose only. All the spectral results presented hereafter were obtained by fitting spectral datasets from different cameras jointly.

The redshift determination was principally driven by the Fe K edge, which is assumed to arise from cold medium and

thus at the energy of 7.1 keV, as it is normally statistically more robust feature than the line. Two exceptions are PID 116 and PID 352, for which the Fe K emission-lines, detected at 2.5σ with $EW \approx 0.15$ keV and 4.5σ with $EW \approx 0.30$ keV, respectively, were used to obtain the redshifts assuming the rest-frame line energy of 6.4 keV emitted from cold matter.

This assumption may not be true for PID 116, which is a luminous submillimetre galaxy detected at $870 \, \mu$m with LABOCA (LESS 9, Wardlow et al. 2011; Biggs et al. 2011). As the X-ray detected luminous infrared galaxies with $L_{IR} \sim 10^{13} \, L_\odot$ at $z > 2$ in the COSMOS field appears to show high-ionization Fe K emission, e.g., Fe XXV at 6.70 keV and/or Fe XXVI at 6.97 keV as inferred from a spectral stacking analysis (Iwasawa et al. 2012), the emission line of PID 116 could also be either of these high-ionization lines. In this case, the redshift would be $z = 3.96$ or $z = 4.16$, when it was identified with Fe XXV and Fe XXVI, respectively. The former value is close to the photometric redshift derived by Luo et al. (2010) and the latter to the secondary solution of Wardlow et al. (2011, see Table 3).

As shown in Table 3, z_X are found to lie within the range of various photometric redshifts.

3.3. 9–20 keV excess sources

The spectra of the seven objects in the V category are shown in Figs. 5 and 6. For displaying purpose, EPIC pn, EPIC MOS1, MOS2, and the *Chandra* data from the ACIS detector are combined together. All the spectra show spectral discontinuities at 6−7 keV, indicating an Fe K line and/or a deep Fe K absorption edge, in agreement with strong absorption.

To estimate the absorbing column density of these sources, an absorbed power-law model with photon index of $\Gamma = 1.8$ is fitted (Table 4). The absorption model with the Wisconsin cross section (Morrison & McCammon 1983) and the one with the effects of Compton scattering taken into account, PLCABS (Yaqoob 1997), give consistent results on N_H. Whilst the absorption cut-off is slightly modified when Compton scattering is taken into account, the 7−20 keV spectrum, shaped by an Fe K edge, remains unchanged in shape for the N_H range of our sources, $N_H \leq 10^{24}$ cm^{-2} (although the flux is further suppressed). This also applies to recently developed more sophisticated X-ray spectral models (e.g., Ikeda et al. 2009; Murphy & Yaqoob 2010). As our N_H fits are mainly driven by the data in the Fe K edge band, it can be understood that both absorption models gives similar N_H, given the data quality of the spectra. However, since Compton scattering reduces the continuum level further compared to the case where the scattering effect is not taken into account, the absorption correction factor for estimating an intrinsic continuum luminosity would be larger. This effect also depends on the geometry of the absorber (e.g., Matt et al. 1999b) which is not known for our objects. In Table 4, we give absorption-correction factors for a spherical absorber. These factors could go up by a factor of ∼2 as the covering factors decreases down to that of a disk-like geometry for the relevant range of N_H.

The column densities given in Table 4 were obtained, assuming the observed emission is transmitted light through an absorber. However, the hard X-ray colour exhibited by these objects could also result from a reflection-dominated spectrum of a Compton thick source. This is probably the case for PID 114, in which a strong Fe K line is detected (see below and Table 5), whereas the apparently moderate column density is inferred from the absorption model for the poor quality continuum spectrum (Table 4). PID 252 has the hardest spectrum in terms of the
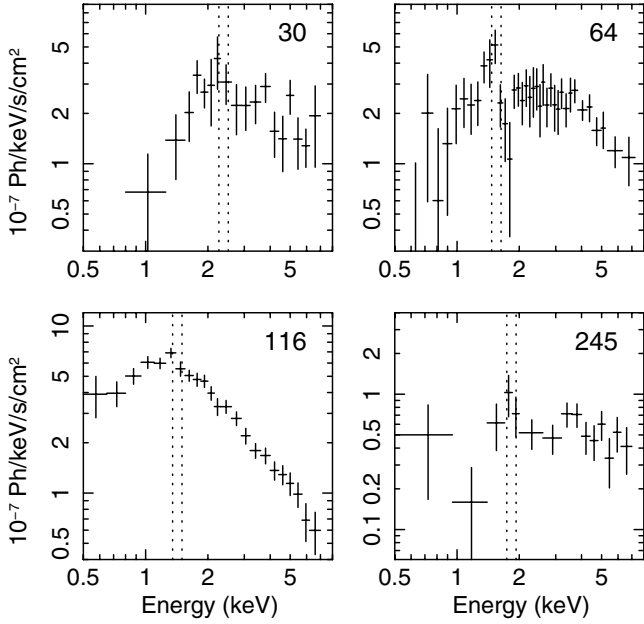
Fig. 5. X-ray spectra of the four objects (PID 30, 64, 116, 245) whose redshifts were determined using the Fe K features. The *Chandra* ACIS-I data, obtained in the deep CDFS (4 Ms) and the ECDFS observations, were combined with the *XMM-Newton* data. The rest-frame 6.4 keV and 7.1 keV which would be observed with those redshifts are indicated by the dotted lines. PID 30, 64, and 245 are heavily obscured sources in the V category while PID 116 is a source in the A category.
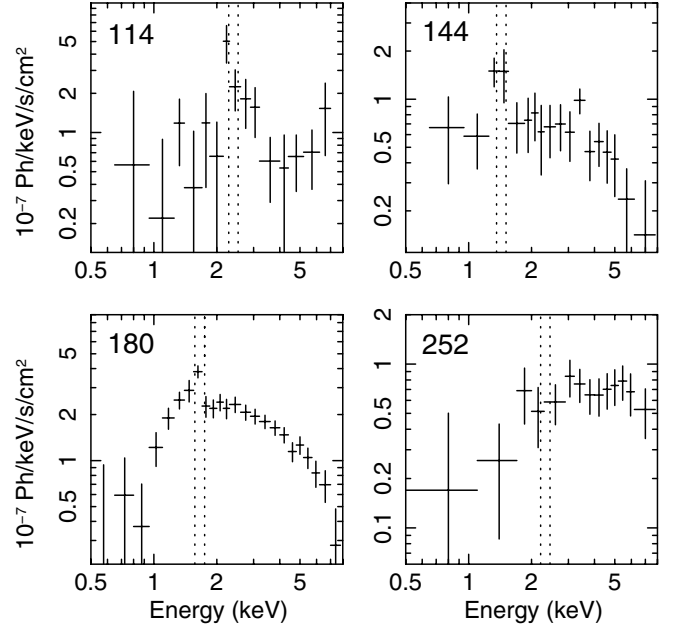
Fig. 6. X-ray spectra of the four objects (PID 114, 144, 180, 252) which complete the seven objects of the V category in addition to the three objects shown in Fig. 5. The rest-frame 6.4 keV and 7.1 keV are indicated by the dotted lines that were computed assuming the spectroscopic redshifts for respective objects.

Table 4. X-ray absorption in the $9-20$ keV excess sources.

PID (1)	$N_{H,24}$ (2)	AC_{2-10} (3)	AC_{10-20} (4)
30	$0.57^{+0.07}_{-0.06}$	7	1.5
64	$0.83^{+0.05}_{-0.04}$	12	1.9
114[†]	$0.40^{+0.15}_{-0.10}$	4	1.3
144	$0.81^{+0.06}_{-0.06}$	11	1.9
180	$0.55^{+0.03}_{-0.02}$	6	1.5
245	$0.96^{+0.09}_{-0.08}$	15	2.1
252[†]	$0.97^{+0.11}_{-0.09}$	16	2.1

Notes. (1) Source identification number; (2) absorption column density in unit of 10^{24} cm^{-2}; (3) absorption correction factor for the $2-10$ keV luminosity; (4) absorption correction factor for the $10-20$ keV luminosity. Spectral fits were performed for the observed-frame $1-7$ keV data using an absorbed power-law with $\Gamma = 1.8$. When a Thomson opacity approaches unity, as observed in these sources, the absorption correction depends on the geometry of absorbing clouds (e.g., Matt et al. 1999b). In this table, the values for a spherical geometry are given as the lower limits. These values can go up by a factor of ~2, as the covering factor of the absorber is reduced. [†] The spectra of these sources can also be described well by a reflection spectrum from cold matter.

hard X-ray colour h/m (Fig. 6) although no obvious Fe line is seen. For these two objects, a pure reflection spectrum from cold matter, modelled by `pexrav` (Magdziarz & Zdziarski 1995) or `pexmon` (Nandra et al. 2007), provides a comparable fit to their spectra, compared to the absorption model. This indicates that these two objects might be Compton thick AGN with a larger N_H than that given in Table 4, e.g., ~10^{25} cm^{-2}.

Fe K emission is detected at ~2σ or larger significance in these objects except for PID 252 (Table 5, see also Comastri et al. 2011). The spectrum of PID 252 does not show clear

Table 5. Fe K line equivalent widths of the V category objects.

| PID	EW_1 keV	EW_2 keV
30	0.76 ± 0.24	0.51 ± 0.19
64	0.57 ± 0.19	0.27 ± 0.11
114	1.40 ± 0.61	1.09 ± 0.53
144	1.13 ± 0.51	0.47 ± 0.23
180	0.65 ± 0.16	0.34 ± 0.12
245	1.10 ± 0.48	0.44 ± 0.28
252	≤ 0.5	≤ 0.2

Notes. EW_1 and EW_2 are measured with respect to the rest-frame $5-10$ keV continuum modelled by a simple power-law and an absorbed power-law of $\Gamma = 1.8$, respectively. For PID 252, 2σ upper limits are given. We remark that EW_2 are always smaller than EW_1 since part of the line is accounted for by the sharp continuum feature of an absorbed continuum carved by an Fe K edge.

Fe K emission with $EW \leq 0.5$ keV (2σ upper limit of a narrow line at 6.4 keV). This weak-line source may be a high-redshift analogue of Mrk 231, a Compton thick AGN with a weak Fe K line in the local Universe (e.g., Braito et al. 2004; Gallagher et al. 2002; Iwasawa et al. 2011, and other references therein). The large EW observed in PID 114 (Table 5) agrees with an Fe K line expected from a reflection-dominated spectrum from cold medium, giving a support to the possibility of a Compton thick source.

4. Discussion

4.1. X-ray selection of heavily obscured AGN

Seven heavily obscured active galaxies with $N_H \geq 0.6 \times 10^{24}$ cm^{-2}, including one previously known source (PID 144, Norman et al. 2002; Comastri et al. 2011), were selected by the rest-frame X-ray colour selection, primarily utilizing the
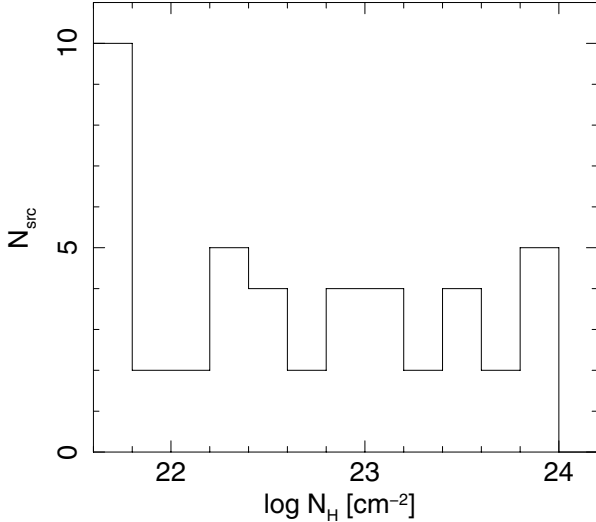
Fig. 7. Distribution of absorbing column density N_H, obtained by fitting an absorbed power-law to the EPIC spectra. The lowest bin represents the number of objects with no detection of absorption. The typical error bar of each bin is ±1.

excess emission in the 9–20 keV band relative to emission at lower energies. Two of them (PID 114 and PID 252) are possibly Compton thick AGN with a reflection-dominated spectrum. Given the limited bandpass available from *XMM-Newton*, this selection can be applied only for high redshift objects, but the a posteriori checks showed that this selection is reliable for sources with spectra of reasonable quality, and can pick up strongly absorbed sources with near Thomson-thick opacity.

This method is a pure X-ray selection, and these seven objects compose a sample of heavily obscured, moderate-luminosity quasars with $L_{10-20} \sim 10^{44}$ erg s^{-1}, selected by the hard X-ray emission above 10 keV beyond the local Universe.

There are various reports in the literature on Compton thick AGN candidates in the CDFS using whole or part of the *Chandra* 4 Ms data (e.g., Norman et al. 2002; Mainieri et al. 2005; Tozzi et al. 2006; Fiore et al. 2008; Gilli et al. 2011; Feruglio et al. 2011; Luo et al. 2011; Brightman & Ueda 2012; Fiore et al. 2012). Some of them lie in the redshift range of our sample, although they are expectedly faint and just a few of them entered in our sample of relatively bright sources. Fiore et al. (2012) investigated high-redshift sources at $z > 3$ in CDFS and selected several heavily obscured AGN. Their E537 (=PID 245), M5390 (=PID 144), M8273 (PID 180), M3320 (=PID107) and M4302 (=PID 120) are in our sample. Our results on the spectra of these sources agree except for PID 120 for which only moderate absorption of $N_H = 1.6^{+0.5}_{-0.6} \times 10^{22}$ cm^{-2} is found. The smaller N_H value for PID 245 obtained by us (Table 4) is explained by the lower redshift adopted for this source: the X-ray redshift $z_X = 2.68$ (Sect. 3.2, Table 3), instead of the photometric redshift $z = 4.29$ from the GOODS-ERS (Grazian et al. 2011) adopted by Fiore et al. (2012), which a close inspection of the X-ray/optical/infrared images suggests to be the redshift for another galaxy near the X-ray source.

4.2. Absorbed AGN fraction

In Fig. 3, when the model locus is used as a guide, 10 objects appear to have *unobscured* X-ray sources, i.e., their X-ray absorption is $N_H < 10^{22}$ cm^{-2}. That is, ~3/4 of our sample objects host significantly obscured active nuclei. Fitting to the

individual spectra verifies the above assessment with 12 objects having N_H values smaller than 10^{22} cm^{-2}, and gives the N_H distribution shown in Fig. 7. The distribution of $\log N_H$ (cm^{-2}) is nearly flat between 22−24, although the two objects (PID 114 and 252) possibly move up to $\log N_H > 24$ (cm^{-2}). For their typical 2−10 keV intrinsic luminosities $[(0.8−5)\times10^{44}$ erg s$^{-1}]$, these active galaxies at $z \sim 2.5$ can all be considered to emit at quasar luminosity, and 74 ± 8 per cent of them are absorbed X-ray sources. We have estimated this absorbed AGN fraction using a Bayesian approach and the binomial distribution (Wall & Jenkins 2008) with a 68 per cent confidence interval (Andreon, priv. comm.). It should be noted that, since the fraction of Compton thick AGN is not constrained, this value is considered to be the lower limit of the absorbed AGN fraction.

We compared our findings with the predictions of the XRB synthesis model by Gilli et al. (2007). Our sample spans the 2−10 keV flux range $(2−54)\times10^{-15}$ erg cm^{-2} s^{-1}. Since the sensitivity of the XMM-CDFS observations strongly varies across the field, we computed the model predictions at the 2−10 keV limiting flux, $f^{lim}_{2-10} = 4 \times 10^{-15}$ erg cm^{-2} s^{-1}, which returns the same AGN surface density of our sample, i.e. 46 sources at $z > 1.7$ distributed over a ~0.27 deg^2 area. The predicted obscured fraction (defined as the number of AGN with $\log N_H > 22$ over the total number of AGN in the sample) is 0.54 ± 0.06, smaller than the observed value of 0.74 ± 0.08.

In the local Universe, the *Swift*/BAT and INTEGRAL surveys show that absorbed sources (with $N_H > 10^{22}$ cm^{-2}) consist ~55 per cent of hard X-ray selected AGN (e.g., Burlon et al. 2011, and references therein). It is also found that this fraction depends on X-ray luminosity, and at the luminosity matched to our sample, the fraction is 21 ± 8 per cent (Burlon et al. 2011, see also Ebrero et al. 2008). The absorbed quasar fraction ($L^{int}_{2-10} \geq 10^{44}$ erg s^{-1}) in our sample is higher than that of the local Universe, suggesting a positive evolution with redshift, as found in the previous work by La Franca et al. (2005), Treister & Urry (2006) and Ebrero et al. (2008). No evolution of the obscured AGN fraction was assumed in Gilli et al. (2007), yet the prediction comes close to the observation at $z > 1.7$ as discussed above. However, we note that the luminosity dependence of the obscured AGN fraction assumed in Gilli et al. (2007) appears to be shallower than the observations (Hasinger 2008; Brusa et al. 2010; Burlon et al. 2011), and it overestimates the obscured fraction of quasi-stellar objects (QSOs) with $L_{2-10} > 10^{44}$ erg s^{-1} in the local Universe by a factor of ~2.5. This excess number assumed for local obscured QSOs then compensates the lack of a redshift evolution of their fraction in the model.

Contrary to the high-luminosity AGN, no strong evidence for a redshift dependence of the obscured AGN fraction at luminosities <10^{44} erg s^{-1} has been found. Gilli et al. (2010), for instance, showed that the increasing trend of the absorbed fraction *as observed* by Hasinger (2008) for AGN with $L_{2-10} \leq 10^{44}$ erg s^{-1}, can be accounted for by the K-correction effect, and is instead consistent with a non-evolving *intrinsic* absorbed fraction. Here we suggest that the obscured fraction increases with redshift *only* for luminous QSOs. The different behaviours in obscured fraction between low- and high-luminosity AGN may reflect their distinct accretion mechanisms, as argued in literature (Hasinger 2008; Hopkins et al. 2008; Hickox et al. 2009): merger-driven accretion for luminous AGN (e.g., Menci et al. 2008) and secular accretion for less luminous AGN, possibly mirroring their respective drivers of star formation (e.g., Elbaz et al. 2011). This may not be the whole story but qualitatively explains the different bahaviours between AGN of the low and high luminosity ranges. If all QSOs originate from a major merger of gas-rich

galaxies (e.g., Sanders et al. 1988), the increase of merger rate at high redshift (with $\propto (1 + z)^2$, e.g., Xu et al. 2012) naturally sees an increase in number of QSOs. A merger causes gas channelling to the nuclear region (Barnes & Hernquist 1991). This concentration of gas and the chaotic geometry left by a merger would lead to a high probability of the nuclear region to be seen obscured (e.g., Hopkins et al. 2006; but see Shawinski et al. 2012) until the radiation pressure of the buried QSO sweeps it away. In the context of this evolutionary scenario alone, the obscured fraction of QSOs is expected to be constant at all redshift, given the short duration of the QSO lifetime ($\leq 10^8$ yr, Hopkins et al. 2005). The evolution we observed is probably driven by the increase in the gas fraction of a galaxy towards high redshift (e.g., Carilli et al. 2011), combined with the efficient inflow induced by a merger. A higher gas fraction of merger progenitor galaxies means more gas to be transported to the nuclear region to form heavier obscuration. This would result in a longer duration of the obscured phase, which can be translated to a higher obscured fraction of the QSO population at high redshift. At the same time, the elevated gas density by a merger increases the efficiency of star formation leading to a starburst (e.g., Barnes & Hernquist 1991; Elbaz et al. 2011). Kinetic energy injection from a starburst may help to maintain the obscuration by inflating gaseous wall around AGN (e.g., Fabian et al. 1998). Conversely, the lack of mergers may explain the little evolution of the obscured fraction in lower luminosity AGN. The gas fraction of galaxies hosting them also increases towards high redshift in the same way as for high-luminosity AGN. However, without a major merger, the gas reservoir is not transported to the nuclear region rapidly. This means that the nuclear obscuration condition remains little affected regardless the amount of gas contained in a galaxy (hence redshifts). The gas content is instead consumed to form stars over galaxy-wide as a secular process, and the feeding to the black hole from a large-scale disk remains relatively inefficient.

In summary, we present a result of a rest-frame $9-20$ keV selection of heavily obscured AGN at $z > 1.7$, using the deep XMM-CDFS survey, and also show that the fraction of absorbed AGN at high luminosity may be higher at high redshift than in the local Universe. In the near future, a further advance in this area of research will benefit from even deeper observations of deep fields with *Chandra* and *XMM-Newton*, while NuSTAR and Astro-H which will provide us with useful templates and insights at lower redshifts. It is also useful to standardize various X-ray spectral models of strongly absorbed systems with improved physics incorporated for the community to share with.

References

Alexander, D. M., Bauer, F. E., Brandt, W. N., et al. 2011, ApJ, 738, 44
Alonso-Herrero, A., Pérez-González, P. G., Alexander, D. M., et al. 2006, ApJ, 640, 167
Balestra, I., Mainieri, V., Popesso, P., et al. 2010, A&A, 512, A12
Barnes, J. E., & Hernquist, L. E. 1991, ApJ, 370, L65
Bauer, F. E., Yan, L., Sajina, A., & Alexander, D. M. 2010, ApJ, 710, 212
Biggs, A. D., Ivison, R. J., Ibar, E., et al. 2011, MNRAS, 413, 2314
Braito, V., Della Ceca, R., Piconcelli, E., et al. 2004, A&A, 420, 79
Brandt, W. N., Iwasawa, K., & Reynolds, C. S. 1996, MNRAS, 281, L41
Brightman, M., & Ueda, Y. 2012, MNRAS, 423, 702

Brusa, M., Civano, F., Comastri, A., et al. 2010, ApJ, 716, 348
Burlon, D., Ajello, M., Greiner, J., et al. 2011, ApJ, 728, 58
Carilli, C. L., Walter, F., Riechers, D., et al. 2011 [arXiv:1105.1128]
Cooper, M. C., Yan, R., Dickinson, M., et al. 2012, MNRAS, 425, 2116
Cardamone, C. N., Urry, C. M., Damen, M., et al. 2008, ApJ, 680, 130
Comastri, A., Ranalli, P., Iwasawa, K., et al. 2011, A&A, 526, L9
Daddi, E., Alexander, D. M., Dickinson, M., et al. 2007, ApJ, 670, 173
Dahlen, T., Mobasher, B., Dickinson, M., et al. 2010, ApJ, 724, 425
Dickey, J. M., & Lockman, F. J. 1990, ARA&A, 28, 215
Donley, J. L., Koekemoer, A. M., Brusa, M., et al. 2012, ApJ, 748, 142
Ebrero, J., Carrera, F. J., Page, M. J., et al. 2009, A&A, 493, 55
Elbaz, D., Dickinson, M., Hwang, H. S., et al. 2011, A&A, 533, A119
Fabian, A. C., Barcons, X., Almaini, O., & Iwasawa, K. 1998, MNRAS, 297, L11
Feruglio, C., Daddi, E., Fiore, F., et al. 2011, ApJ, 729, L4
Fiore, F., Grazian, A., Santini, P., et al. 2008, ApJ, 672, 94
Fiore, F., Puccetti, S., Brusa, M., et al. 2009, ApJ, 693, 447
Fiore, F., Puccetti, S., Grazian, A., et al. 2012, A&A, 537, A16
Gallagher, S. C., Brandt, W. N., Chartas, G., Garmire, G. P., & Sambruna, R. M. 2002, ApJ, 569, 655
George, I. M., & Fabian, A. C. 1991, MNRAS, 249, 352
Giacconi, R., Zirm, A., Wang, J., et al. 2002, ApJS, 139, 369
Gilli, R., Comastri, A., & Hasinger, G. 2007, A&A, 463, 79
Gilli, R., Comastri, A., Vignali, C., Ranalli, P., & Iwasawa, K. 2010, X-ray Astronomy 2009, Present Status, Multi-Wavelength Approach and Future Perspectives, 1248, 359
Gilli, R., Su, J., Norman, C., et al. 2011, ApJ, 730, L28
Grazian, A., Castellano, M., Koekemoer, A. M., et al. 2011, A&A, 532, A33
Guainazzi, M., Matt, G., Brandt, W. N., et al. 2000, A&A, 356, 463
Hasinger, G. 2008, A&A, 490, 905
Hickox, R. C., Jones, C., Forman, W. R., et al. 2009, ApJ, 696, 891
Hopkins, P. F., Hernquist, L., Martini, P., et al. 2005, ApJ, 625, L71
Hopkins, P. F., Hernquist, L., Cox, T. J., et al. 2006, ApJS, 163, 1
Hopkins, P. F., Hernquist, L., Cox, T. J., & Kereš, D. 2008, ApJS, 175, 356
Ikeda, S., Awaki, H., & Terashima, Y. 2009, ApJ, 692, 608
Iwasawa, K., Sanders, D. B., Teng, S. H., et al. 2011, A&A, 529, A106
Iwasawa, K., Koyama, K., Awaki, H., et al. 1993, ApJ, 409, 155
Iwasawa, K., Mainieri, V., Brusa, M., et al. 2012, A&A, 537, A86
La Franca, F., Fiore, F., Comastri, A., et al. 2005, ApJ, 635, 864
Lehmer, B. D., Brandt, W. N., Alexander, D. M., et al. 2005, ApJS, 161, 21
Luo, B., Brandt, W. N., Xue, Y. Q., et al. 2010, ApJS, 187, 560
Luo, B., Brandt, W. N., Xue, Y. Q., et al. 2011, ApJ, 740, 37
Magdziarz, P., & Zdziarski, A. A. 1995, MNRAS, 273, 837
Mainieri, V., Rigopoulou, D., Lehmann, I., et al. 2005, MNRAS, 356, 1571
Marconi, A., Risaliti, G., Gilli, R., et al. 2004, MNRAS, 351, 169
Martínez-Sansigre, A., Rawlings, S., Lacy, M., et al. 2005, Nature, 436, 666
Matt, G., Guainazzi, M., Frontera, F., et al. 1997, A&A, 325, L13
Matt, G., Guainazzi, M., Maiolino, R., et al. 1999a, A&A, 341, L39
Matt, G., Pompilio, F., & La Franca, F. 1999b, New Astron., 4, 191
Menci, N., Fiore, F., Puccetti, S., & Cavaliere, A. 2008, ApJ, 686, 219
Morrison, R., & McCammon, D. 1983, ApJ, 270, 119
Murphy, K. D., & Yaqoob, T. 2009, MNRAS, 397, 1549
Nandra, K., O'Neill, P. M., George, I. M., & Reeves, J. N. 2007, MNRAS, 382, 194
Norman, C., Hasinger, G., Giacconi, R., et al. 2002, ApJ, 571, 218
Popesso, P., Dickinson, M., Nonino, M., et al. 2009, A&A, 494, 443
Rafferty, D. A., Brandt, W. N., Alexander, D. M., et al. 2011, ApJ, 742, 3
Sanders, D. B., Soifer, B. T., Elias, J. H., et al. 1988, ApJ, 325, 74
Santini, P., Fontana, A., Grazian, A., et al. 2009, A&A, 504, 751
Schawinski, K., Simmons, B. D., Urry, C. M., Treister, E., & Glikman, E. 2012, MNRAS, 425, L61
Silverman, J. D., Mainieri, V., Salvato, M., et al. 2010, ApJS, 191, 124
Szokoly, G. P., Bergeron, J., Hasinger, G., et al. 2004, ApJS, 155, 271
Taylor, E. N., Franx, M., van Dokkum, P. G., et al. 2009, ApJS, 183, 295
Tozzi, P., Gilli, R., Mainieri, V., et al. 2006, A&A, 451, 457
Treister, E., & Urry, C. M. 2006, ApJ, 652, L79
Treister, E., Urry, C. M., & Virani, S. 2009a, ApJ, 696, 110
Treister, E., Virani, S., Gawiser, E., et al. 2009b, ApJ, 693, 1713
Vignati, P., Molendi, S., Matt, G., et al. 1999, A&A, 349, L57
Vignali, C., Alexander, D. M., Gilli, R., & Pozzi, F. 2010, MNRAS, 404, 48
Wall, J. V., & Jenkins, C. R. 2003, Practical Statistics for Astronomers (CUP), 21
Wardlow, J. L., Smail, I., Coppin, K. E. K., et al. 2011, MNRAS, 415, 1479
Wuyts, S., Labbé, I., Schreiber, N. M. F., et al. 2008, ApJ, 682, 985
Xu, C. K., Zhao, Y., Scoville, N., et al. 2012, ApJ, 747, 85
Xue, Y. Q., Luo, B., Brandt, W. N., et al. 2011, ApJS, 195, 10
Yaqoob, T. 1997, ApJ, 479, 184